

Temperature-compensated fiber Bragg grating pressure sensor utilizing square diaphragm-based stress transfer structure

Qinggeng Fan(樊庆赓), Dequan Feng(冯德全), Zhen'an Jia(贾振安), and Muguang Wang(王目光)
Citation: Chin. Phys. B, 2026, 35 (**4**): 044206. DOI: 10.1088/1674-1056/ae0162
http://cpb.iphy.ac.cn; http://iopscience.iop.org/cpb

What follows is a list of articles you may be interested in

Full stabilization of eight-channel Yb-fiber coherent beam combining system delivering 1.18-kW, 1.18-mJ, 270-fs pulses

Zhuo Shi(史卓), Zhi-Hang Du(杜志航), Cheng-Bin Liang(梁成斌), Hong-Xiang Chang(常洪祥), Zi-Kai Dong(董自凯), Hong-Yu Guo(郭鸿宇), Can Li(李灿), Pu Zhou(周朴), Zhi-Yi Wei(魏志义), and Guo-Qing Chang(常国庆)
Chin. Phys. B, 2026, 35 (**2**): 024210. DOI: 10.1088/1674-1056/ae1952

Single-frequency linearly polarized *Q*-switched fiber laser based on Nb_2GeTe_4 saturable absorber

Si-Yu Chen(陈思雨), Hai-Qin Deng(邓海芹), Wan-Ru Zhang(张万儒), Yong-Ping Dai(戴永平), Tao Wang(王涛), Qiang Yu(俞强), Can Li(李灿), Man Jiang(姜曼), Rong-Tao Su(粟荣涛), Jian Wu(吴坚), and Pu Zhou(周朴)
Chin. Phys. B, 2023, 32 (**7**): 074203. DOI: 10.1088/1674-1056/acad6d

An approach to gas sensors based on tunable diode laser incomplete saturated absorption spectra

Wei Nie(聂伟), Zhen-Yu Xu(许振宇), Rui-Feng Kan(阚瑞峰), Mei-Rong Dong(董美蓉), and Ji-Dong Lu(陆继东)
Chin. Phys. B, 2021, 30 (**6**): 064213. DOI: 10.1088/1674-1056/abd769

Hollow and filled fiber bragg gratings in nano-bore optical fibers

Yong-Xin Zhang(张永欣), Sheng Liang(梁生), Qian-Qing Yu(余倩卿), Zheng-Gang Lian(廉正刚), Zi-Nian Dong(董梓年), Xuan Wang(王旋), Yu-Qin Lin(林裕勤), Yu-Qi Zou(邹郁祁), Kun Xing(邢坤), Liu-Yan Liang(梁柳雁), Xiao-Ting Zhao(赵小艇), Li-Jing Tu(涂立静)
Chin. Phys. B, 2019, 28 (**7**): 074210. DOI: 10.1088/1674-1056/28/7/074210

Wavelength modulation spectroscopy at 1530.32 nm for measurements of acetylene based on Fabry-Perot tunable filter

Yun-Long Li(李运龙), Bing-Chu Yang(杨兵初), Xue-Mei Xu(许雪梅)
Chin. Phys. B, 2016, 25 (**2**): 024208. DOI: 10.1088/1674-1056/25/2/024208

Temperature-compensated fiber Bragg grating pressure sensor utilizing square diaphragm-based stress transfer structure

Qinggeng Fan(樊庆赓)[1], Dequan Feng(冯德全)[2], Zhen'an Jia(贾振安)[2], and Muguang Wang(王目光)[1,†]

[1] *Institute of Lightwave Technology, Key Laboratory of All Optical Network and Advanced Telecommunication Network, Ministry of Education, Beijing Jiaotong University, Beijing* 100044, *China*

[2] *Ministry of Education Key Laboratory on Photoelectric Oil–Gas Logging and Detecting, School of Science, Xi'an Shiyou University, Xi'an* 710065, *China*

(Received 24 June 2025; revised manuscript received 20 August 2025; accepted manuscript online 2 September 2025)

A fiber Bragg grating (FBG) pressure sensor using square diaphragm, dowel bar, and constant-strength cantilever beam (CSCB) as the stress transfer structure is proposed in this paper. The measurement principle involving pressure to strain transduction is described. Comparative finite element simulations of two diaphragms show square diaphragm's superior pressure responsivity, demonstrating a central deflection approximately 30% greater than that of the circular diaphragm. The performance of this design over the range of 0 to 2 MPa is experimentally evaluated, achieving a pressure sensitivity of 273.72 pm/MPa, excellent coefficient of determination (R^2) of 0.9992, 0.688% full scale (FS) hysteresis, and 3.368% FS repeatability errors. Furthermore, the utilization of difference in central wavelength shifts between dual Bragg gratings enables effective temperature compensation, resulting in a relative error of 2%. The cost-effective sensor can be adopted for the pressure measurement of gases or liquids within pipelines.

Keywords: pressure sensor, fiber Bragg grating (FBG), square diaphragm, temperature compensation

PACS: 42.81.–i, 07.07.Df, 47.80.Fg, 07.60.Vg

DOI: 10.1088/1674-1056/ae0162 **CSTR:** 32038.14.CPB.ae0162

1. Introduction

Long-distance oil and gas pipelines, such as those used for the transportation of petroleum and natural gas, are subject to challenges arising from their vast scale, complex environmental conditions, and prolonged operation. These include pressure fluctuations due to fluid dynamics, localized structural degradation caused by corrosion, and the critical need for early leakage detection to ensure environmental and operational safety.[1] Traditional electrical pressure sensors are not well-suited for such demanding conditions, as they are difficult to install, susceptible to electromagnetic interference, and limited in signal transmission distance. Moreover, intensity modulation-based[2] and interferometric[3] optical pressure sensors are often sensitive to light source fluctuations, as well as environmental factors such as temperature, vibration, and mechanical disturbances, which can lead to long-term instability and measurement errors. In particular, interferometric sensors are associated with complex fabrication processes and relatively high costs, further limiting their practical application.

Fiber Bragg grating (FBG), with its high sensitivity, immunity to electromagnetic interference, and capability for absolute measurements, exhibits excellent adaptability to diverse environmental conditions, making it an ideal solution to these challenges.[4] The FBG enables detection of diverse physical parameters including stress/strain,[5] temperature,[6] magnetic fields,[7] and vibration acceleration.[8] Moreover, the chirped FBG variant, characterized by an axially varying refractive index modulation period, functions as a dispersion compensation element.[9]

Bare FBGs exhibit weak sensitivity to external pressure,[10] hence requiring specially designed structures to enhance pressure response while protecting the grating from mechanical damage. Circular diaphragm was preferred for the primary sensing element in fiber-optic sensors of existing studies.[11–13] Fajkus *et al.*[14] leveraged three-dimensional (3D) printing technology to manufacture an FBG pressure sensor with a circular membrane structure. However, the device exhibited a large pressure measurement deviation, with approximately 10% error observed under low-pressure conditions. This may result in a decrease in measurement linearity, thereby affecting the sensor's accuracy. An FBG pressure sensor using circular plate diaphragm recorded a relatively high sensitivity of 3.56 nm/MPa.[15] Despite this, its linear fitting coefficient within the small pressure range of 9 kPa was only 0.9298, indicating potential nonlinearity-induced measurement errors and calibration challenges in practical applications. An analogous sensing approach has similarly been documented.[16,17] Vorathin *et al.*[18] displayed a chirped FBG transducer utilizing a circular rubber diaphragm for low-pressure measurement. In comparison, while Feng *et al.*[19] adapted a metal diaphragm to enable simultaneous

†Corresponding author. E-mail: mgwang@bjtu.edu.cn

© 2026 Chinese Physical Society and IOP Publishing Ltd. All rights, including for text and data mining, AI training, and similar technologies, are reserved.

high-temperature and high-pressure monitoring, this enhanced environmental tolerance came at the cost of reduced sensitivity, reaching only 50.6 pm/MPa. Vaddadi *et al.*[20] proposed a novel structure comprising a metal circular diaphragm and a seesaw hinge mechanism. However, the fulcrum and connections in the seesaw structure, which operate on the lever principle, may exhibit gaps or looseness, resulting in significant measurement hysteresis and repeatability errors. Recently, Liu *et al.*[21] have extended the pressure-sensitive element to a rectangular diaphragm. Although the sensor was designed for high-pressure measurement, the thin diaphragm may experience plastic deformation or even structural failure as the pressure increases.

As is known, FBG exhibits sensitivity to both strain and temperature; therefore, isolating temperature-induced wavelength shifts plays a critical role in practical applications. Liang *et al.*[22] effectively reduced the temperature–pressure cross-sensitivity by using a dual-FBG structure. However, there was a significant difference in the temperature sensitivity coefficients of the two FBGs. This required more elaborate temperature calibration experiments, which increased the difficulty and time cost of sensor calibration. Burhanuddin *et al.*[23] employed three FBGs for the simultaneous measurement of earth pressure, pore pressure while achieving temperature compensation. Despite this, the temperature compensation FBG, which was suspended, lacked adequate mechanical support, rendering it vulnerable to external vibrations or impacts. Such disturbances may induce positional deviations or damage to the FBG, thereby impairing the accuracy of temperature compensation. Other compensation methods, such as using special elastomer materials to counteract the thermal expansion strain of metal,[24] and inducing FBG birefringence through applied transverse stress,[25] can also reduce the measurement interference of temperature on the target parameters.

The square diaphragm is widely used in high-sensitivity and high-precision microelectromechanical systems (MEMS) piezoresistive pressure sensors due to its designed stress distribution, larger effective area, and simple manufacturing process.[26–28] The integration of a square diaphragm into fiber-optic sensors holds considerable research potential. Building on our prior works,[29,30] which utilized square diaphragm to design FBG pressure sensors with diverse configurations, we have expanded the repertoire of sensing elements in fiber-optic sensors and achieved measurable outcomes across distinct pressure regimes. In particular, as reported in our work,[30] the design demonstrated a high pressure-measurement sensitivity, but its applicability is limited to low-pressure ranges of 0 MPa–0.2 MPa, with a relatively high hysteresis error of 1.09%. Furthermore, the large discrepancy between the temperature sensitivity coefficients of the two FBGs results in suboptimal temperature-compensation performance, with a relative error of 3.13%. These limitations underscore the need not only for improved sensor designs but also for a more comprehensive analysis of the intrinsic characteristics of square diaphragm, enabling their advantages to be fully exploited in enhancing pressure-sensing performance.

In this research, we introduce an FBG sensor that is specifically designed for non-intrusive pressure monitoring, particularly in critical infrastructure applications like oil and gas pipeline monitoring. It features a square diaphragm, a centrally located dowel bar, and a constant-strength cantilever beam (CSCB) with two surface-mounted Bragg gratings, all of which collaboratively constitute the stress transfer mechanism for pressure measurement. Finite element simulations indicate that the square diaphragm exhibits deflection 30% greater than that of a circular configuration, consequently demonstrating superior pressure sensitivity. Experimentally, the proposed sensor displays good linearity, low hysteresis of 0.688% in the range of 0 MPa–2 MPa. Temperature compensation is achieved by utilizing the wavelength shift difference of dual Bragg gratings with closely matched thermal sensitivity coefficients, limiting the relative error to 2%, thereby effectively mitigating temperature interference in pressure monitoring.

2. Sensing mechanisms and finite element simulations

2.1. The sensing mechanisms

Figure 1 illustrates the proposed FBG sensor with comprehensive visualization. It consists of a square diaphragm with clamped edges, a protective cover, a dowel bar which is integrally formed with the square and positioned at its center, as well as a CSCB whose free end rests on the terminal of dowel bar while its fixed end is securely fastened to the base via screws. Two FBGs are symmetrically bonded at the central positions along the longitudinal axes on the surfaces of the CSCB. When pressure load is introduced to the diaphragm via the pressure inlet, the pressure differential across both sides of the diaphragm induces deformation, which is then transferred through the dowel bar into mechanical forces applied to the two FBGs. Furthermore, these two forces are equal but opposite, thereby compressing FBG1 mounted on the top surface while elongating FBG2 adhered to the bottom surface of the CSCB. In comparison to a single Bragg grating, the implementation of a dual-grating configuration enhances the strain sensitivity of the sensor by a factor of two. Moreover, both of the gratings are affixed to the same thermally sensitive metallic substrate, ensuring identical temperature sensitivity coefficient. This configuration is of paramount importance for improving temperature measurement sensitivity and enabling effective temperature compensation in FBG pressure sensor.

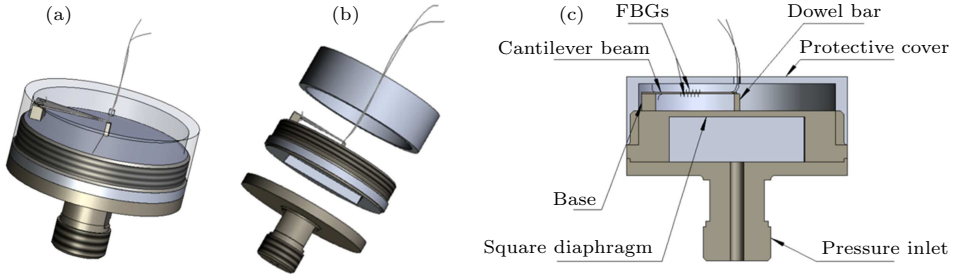


Fig. 1. Pressure sensor configurations: (a) assembled 3D model, (b) exploded diagram, (c) cross-sectional profile.

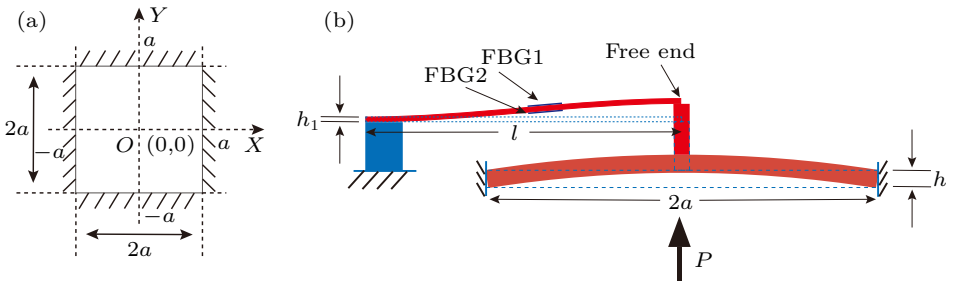


Fig. 2. (a) Structure geometry of square diaphragm with clamped edges, (b) schematic representation of sensor deformation under pressure load. FBG1, attached to the top surface of the CSCB, is compressed under compressive force, resulting in negative strain; while FBG2, positioned symmetrically on the bottom surface of the CSCB, is stretched by tensile force, leading to positive strain. The dashed line indicates the configuration of the stress transfer structure in the absence of the applied pressure load.

Figure 2(a) illustrates the geometry of the square diaphragm with fully clamped edges and an edge dimension of $2a$. Under a uniform pressure load P, the deflection at arbitrary positions across the diaphragm can be described by[31]

$$w(x,y) \cong \frac{1}{47} P \frac{a^4}{U} \left(1 - \frac{x^2}{a^2}\right)^2 \left(1 - \frac{y^2}{a^2}\right)^2, \tag{1}$$

in which U denotes the bending rigidity[32,33]

$$U = \frac{Eh^3}{12(1-\mu^2)}, \tag{2}$$

where E represents the material's Young's modulus, μ signifies its Poisson's ratio, and h stands for its thickness. From Eq. (1), it can be deduced that the deflection occurring at the center of the square is given by

$$w_{\max} = \frac{1}{47} P \frac{a^4}{U}. \tag{3}$$

Figure 2(b) presents schematic diagram of sensor deformation under constant pressure load. According to mechanics of materials, the center deflection of the square converts into the strain of the CSCB, which is written as

$$\varepsilon = \frac{h_1}{l^2} w_{\max}, \tag{4}$$

where h_1 denotes the thickness of the CSCB, and l corresponds to its longitudinal length. Substituting Eqs. (2) and (3) into Eq. (4), the strain of the CSCB caused by applied pressure can be expressed as

$$\varepsilon = \frac{12(1-\mu^2)}{47} \frac{h_1 a^4}{l^2 E h^3} P. \tag{5}$$

As depicted in Fig. 2(b), two commercially available FBGs, with initial wavelength of 1548.713 nm and 1548.1962 nm, respectively, grating length of 1 cm, are bonded to the surface of the CSCB using 502 super glue. The central Bragg wavelength shift $\Delta\lambda_B$, arising from the combined effects of strain ε and temperature change ΔT, is given by[34,35]

$$\Delta\lambda_B = \lambda_B[(1-p_e)\varepsilon + (\alpha+\xi)\Delta T], \tag{6}$$

where p_e, α, and ξ denote the effective photo-elastic coefficient, the thermal expansion coefficient, and the thermal-optic coefficient, respectively. λ_B is the central Bragg wavelength.

Due to their close proximity, the two FBGs are considered to experience identical temperature variations. Additionally, the stress-induced strains in the two FBGs mean that FBG1 experiences compressive strain (negative strain) resulting from compressive force, while FBG2 undergoes tensile strain (positive strain) caused by tensile force. By incorporating the above descriptions, rearranging Eq. (6) allows elimination of the temperature effect

$$\frac{\Delta\lambda_{B2}}{\lambda_{B2}} - \frac{\Delta\lambda_{B1}}{\lambda_{B1}} = 2(1-p_e)\varepsilon. \tag{7}$$

2.2. Simulations for two types of diaphragms

The CSCB is fabricated from beryllium bronze, which offers high strength and good oxidation resistance,[36] while the remaining components utilize economical 6061 aluminum alloy (AA 6061) as the manufacturing material.[37] The dimensional specifications and material properties, as tabulated in Table 1, are consistent in fabrication and the simulations. To

highlight the performance advantages of the square diaphragm employed in this design compared with the conventional circular diaphragm, a comparative finite element analysis is developed using ANSYS Workbench software.

Table 1. Geometric dimensions and material properties used in manufacturing and simulation.

Symbol	Description	Value
$2a$	diaphragm length or diameter	40 mm
h	thickness of square diaphragm	1.7 mm
h_1	thickness of CSCB	0.5 mm
l	length of CSCB	33 mm
	density of AA 6061	2.75 g/cm^3
μ	Poisson's ratio of AA 6061	0.33
E	Young's modulus of AA 6061	68.9 GPa
p_e	photo-elastic coefficient	0.22
	density of beryllium copper	8.3 g/cm^3
	Poisson's ratio of beryllium copper	0.35
	Young's modulus of beryllium copper	128 GPa
	height of dowel bar	5 mm

In this simulation, both diaphragms are assigned identical thickness and material parameters, with the square diaphragm's side length and the circular diaphragm's diameter both set to $2a$. Figure 3 illustrates that, under 1-MPa pressure, the square diaphragm exhibits greater deflections across all positions compared to the circular one. Specifically at the central position (labeled as 20 mm in the diagram), its calculated central deflection is approximately 30% higher than the circular diaphragm's. The simulation results indicate that the square diaphragm has greater responsiveness to external pressure, implying enhanced sensitivity for sensors incorporating it as the pressure-sensitive component.

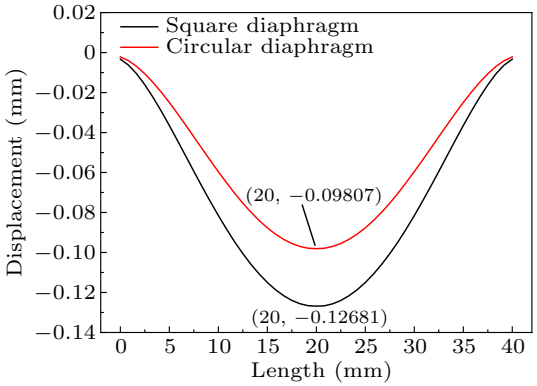


Fig. 3. Displacement of two types of diaphragms under 1 MPa.

A simulation study is also carried out to determine the strain distribution along the longitudinal axis of the CSCB subjected to a 1-MPa pressure load. Figure 4 shows strain values along the CSCB from the free end to the fixed support. Two FBGs are fixed at the 14 mm, where the strain is approximately 1.15×10^{-4}. Two FBGs have nearly identical center wavelengths, thus they are treated as sharing the same value of 1548 nm. Substituting the theoretical strain under 1 MPa into Eq. (7) yields a calculated pressure sensitivity of 277.71 pm/MPa.

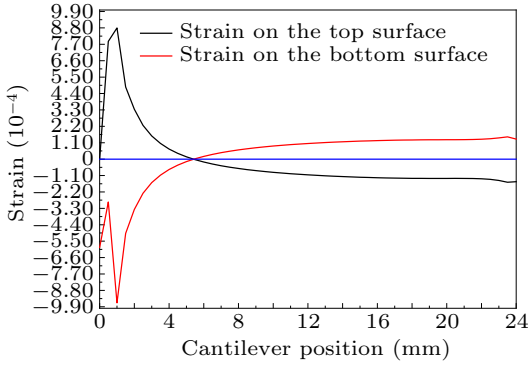


Fig. 4. Surface strain distribution along the longitudinal axis of the CSCB under 1 MPa from the free end.

To make a more comprehensive comparison of the two diaphragms, the simulation is also performed in a large pressure range. Substituting the strain obtained at 14-mm position under diverse pressure into Eq. (7), the wavelength shift difference can be calculated. Figure 5 illustrates that circular and square diaphragm-based pressure sensors exhibit comparable linearity within the range of 0 MPa to 16 MPa. Nonlinear responses emerge as the applied pressure increases further, persisting up to 80 MPa.

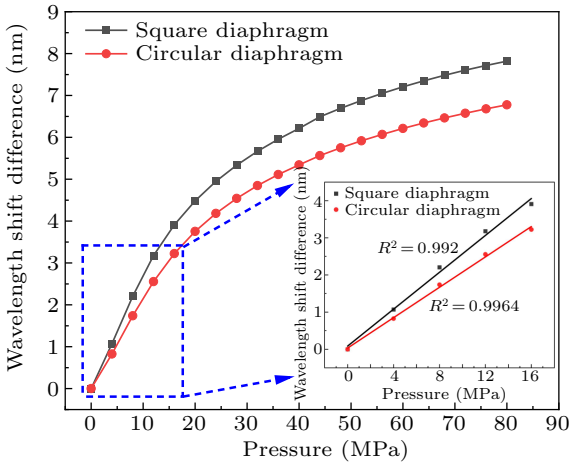


Fig. 5. Comparisons of wavelength shift differences across a wide pressure range for two diaphragms. Inset: coefficient of determination within the range of 0 MPa–16 MPa.

3. Sensor calibration and discussion

3.1. Pressure response characteristics

The pressure experiment is developed at laboratory temperature of 27.6 °C. Figure 6 shows the photograph of the pressure calibration and wavelength interrogation system, alongside this designed sensor. Sensor calibration is performed via a calibrator furnished with a reference pressure gauge (0 MPa–6 MPa range, ±0.25% full-scale accuracy), while the SM125 FBG interrogator captures experimental wavelength data during pressure application.

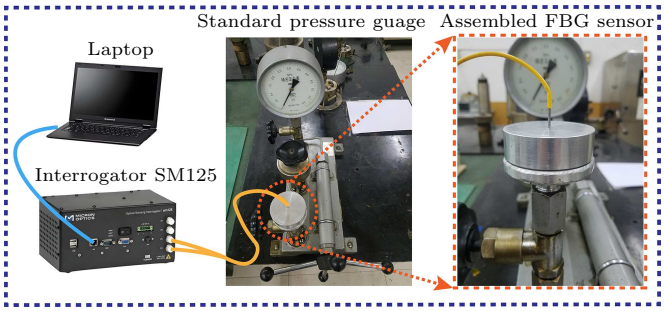


Fig. 6. Photograph of the pressure calibration and wavelength interrogation system, along with the designed FBG pressure sensor.

The proposed sensor's response characteristics are assessed across 0–2 MPa full-scale (FS) with 0.2-MPa increments. From Fig. 7(a), through regression analysis of the measured wavelength data, the pressure sensitivity coefficient is determined to be 273.72 pm/MPa, accompanied by a high coefficient of determination ($R^2 = 0.9992$). Considering the resolution of SM125, which is 1 pm, the pressure resolution is calculated to be 0.0037 MPa. The slight discrepancy between the experimental and theoretical sensitivities arises from the following reasons: First, during the FBGs encapsulation process, adhesive is used to bond the two FBGs to the surface of the CSCB, which may limit the transmission of induced stress. Second, as indicated by the finite element analysis, while a homogeneous strain field is typically assumed along the longitudinal axes at the CSCB's mid-span, slight variations in strain exist at different locations. Consequently, the two FBGs may not bonded to the region of maximum stress on the CSCB. To characterize the sensor's response behavior under repeated pressure variations, three loading-unloading cycles are applied to this design. As depicted in Figs. 7(b) and 7(c), the output data curves demonstrate excellent agreement with each other. Post-calculation analysis reveals a hysteresis error of 0.688% FS and a repeatability error of 3.368% FS.

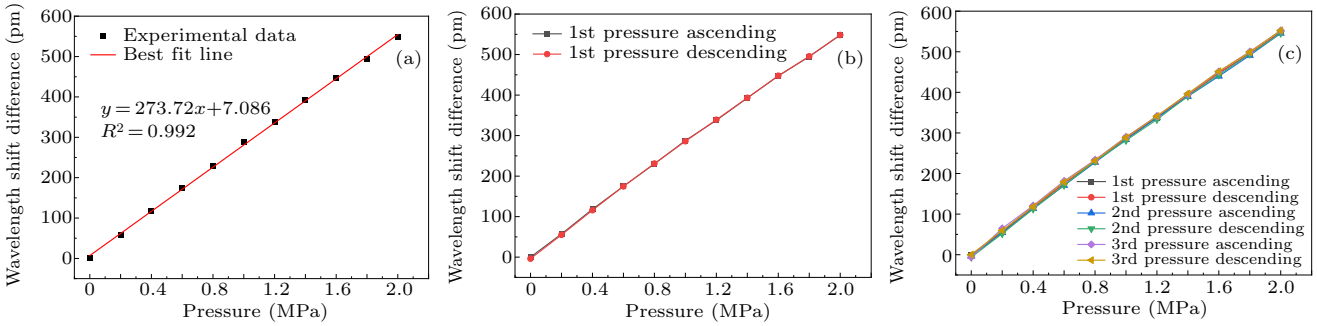


Fig. 7. Critical characteristics of designed sensor: (a) sensitivity, (b) hysteresis, (c) repeatability, illustrated by plotting FBG wavelength shift differences against pressure.

To evaluate the noise characteristics of this design, the wavelengths of the two FBGs at a constant pressure of 1 MPa are recorded once per hour, and this data-recording process persists for a total of nine hours. A maximum wavelength shift difference of 12.9 pm is observed in Fig. 8. Combined with the experimentally determined pressure sensitivity of 273.72 pm/MPa, the accuracy of this designed sensor is calculated to be 0.047 MPa.

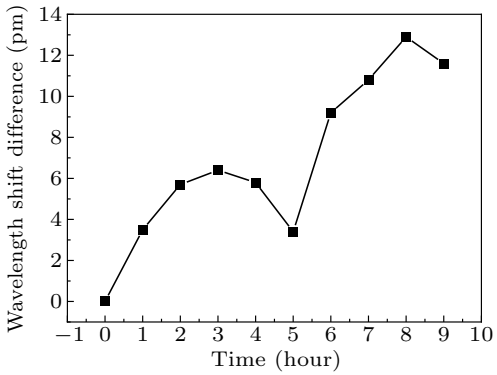


Fig. 8. Wavelength shift difference against time at a steady 1 MPa. The maximum wavelength shift difference is recorded as 12.9 pm, occurring at the eighth hour of the recording period.

3.2. Temperature response characteristics

Under zero-pressure conditions, the correlation between central wavelength shift and controlled temperature variations is characterized using a vacuum drying oven (Make: Taisite, Model: YLD-6000). The sampling interval of temperature is 5 °C between 28 °C to 48 °C. To ensure stable operating conditions during data acquisition, the time interval between each measurement point is configured as approximately 30 minutes. The wavelength shift of the uncompensated pressure sensor under various temperatures obtained from experiment is shown in Fig. 9(a). Evidently, the dual FBGs exhibit thermal sensitivities of 26.47 pm/°C and 25.8 pm/°C for FBG1 and FBG2, respectively, with the coefficients of determination are 0.9934 and 0.9936. The slight difference in their temperature sensitivities can be attributed to small variations in the 502 super glue, including differences in thickness and uniformity. Its low softening temperature, high brittleness, and thermal expansion mismatch with both the fiber and the metallic substrate can affect strain transfer efficiency. In addition, although the gratings are symmetrically attached to the upper and lower surfaces of the beam, the presence of multiple structural materials (aluminum alloy diaphragm, dowel

bar, and beryllium bronze beam) with different coefficients of thermal expansion (CTE) may induce slight variations in local thermal strain transfer at the material interfaces, which can contribute marginally to the observed deviation. By calculating the difference in central wavelength shifts ($\Delta\lambda_{B1} - \Delta\lambda_{B2}$) between the two FBGs at different temperatures, the maximum differential observed at 48 °C is 10.9 pm, as depicted in Fig. 9(b). Given the sensitivity (273.72 pm/MPa) identified from the experimental findings, the measurement error resulting from temperature effects for this design is calculated as 0.04 MPa, accounting for 2% of the entire pressure measurement range.

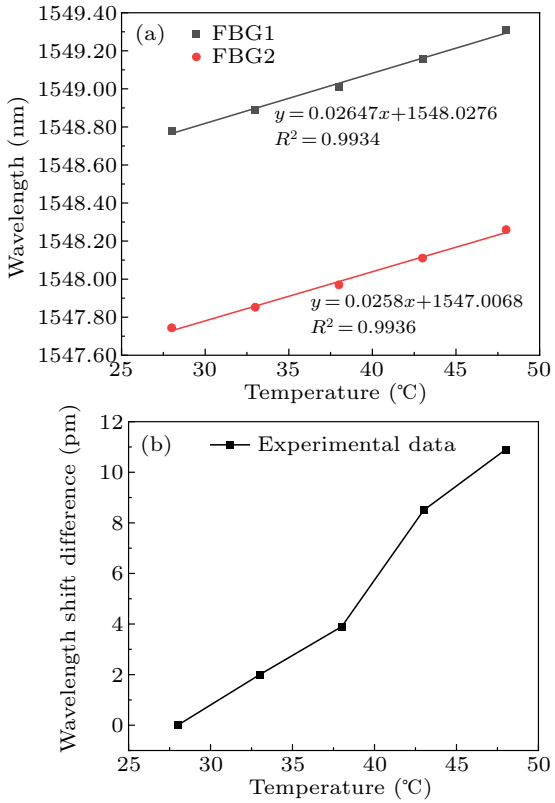


Fig. 9. (a) Wavelength variation of two FBGs *versus* temperature. (b) Temperature-dependent variation of the wavelength shift difference between two FBGs.

3.3. Discussion

Table 2 presents a comparative analysis between this proposed design and reported fiber-optic pressure sensors in terms of pressure sensitivity, measurement range, hysteresis, repeatability, and measurement error after thermal compensation. It can be observed that within the medium pressure range, the hysteresis error of our design demonstrates certain performance advantages. In addition, the measurement error after thermal compensation is reduced to 2% (0.04 MPa), which is consistent with the results reported in existing studies. This agreement confirms the effectiveness of the adopted compensation strategy, while further optimization may still help to reduce error.

(i) Materials with a lower CTE, or those with CTE closely matching that of the FBG, are recommended for integral fabrication of the sensor, thereby eliminating thermal mismatch effects associated with multi-material assemblies.

(ii) Low-creep epoxy could be used for FBG bonding to enhance packaging stability and expand the sensor's temperature response range, thereby ensuring consistent thermal drift between the two FBGs. Ultimately, differential demodulation is implemented to further suppress temperature-induced measurement error.

The repeatability error of 3.368% may be attributed to the hard and brittle nature of 502 adhesive after curing. Under cyclic pressure loading, the adhesive is prone to gradual deformation and stress relaxation, causing the strain perceived by the FBG to vary with the number of loading cycles. Therefore, to reduce this error, an epoxy adhesive with flexibility and excellent fatigue resistance could also be employed as the bonding agent.

The overall dimensions of the designed sensor still have room for further optimization. Future improvements can be made through the following strategies: a high-yield-strength material can be adopted for an integrated structural design, enabling a reduction in diaphragm thickness while increasing the thickness and decreasing the length of the cantilever beam. In addition, an FBG with a shorter grating length (instead of the 10 mm used in this study) could be employed. Furthermore, the height of the dowel bar at the diaphragm center (currently 5 mm) can be reduced to 2 mm or even 1 mm, thereby contributing to a more compact sensor configuration.

Table 2. Comparative evaluation of diverse FBG pressure sensors.

References	Pressure range (MPa)	Pressure sensitivity (pm/MPa)	Hysteresis (%)	Repeatability (%)	Measurement error after thermal compensation (%)
Liu *et al.*[38]	0–1	5227	1.43	2.38	1.04
Hafizi *et al.*[39]	0–0.5	2848.5	–	–	2.32
Liu *et al.*[21]	0–30	30.8714	–	2.7	–
Burhanuddin *et al.*[23]	0–0.0127	6259	–	3.5[a)]	–
Guo *et al.*[40]	0–50	42.47[b)]	–	–	4.65
This work	**0–2**	**273.72**	**0.688**	**3.368**	**2**

[a)]Calculated from standard deviation in vertical pressure.
[b)]Calculated from simulation results at 50 MPa @ 1550 nm.

4. Conclusion

This study presented a novel design and experimental implementation for an FBG-based pressure sensor integrating a square diaphragm, a dowel bar, and a CSCB as the stress transfer structure, accompanied by theoretical analysis with a pressure–strain transfer relationship. Comparative simulations of square and circular diaphragms were developed, indicating enhanced mechanical responsivity in square configuration, particularly demonstrating approximately 30% greater central deflection under equivalent loading conditions, while maintaining comparable linearity to circular geometry across the range of 0–16 MPa. Experimental results showed that the designed pressure sensor achieved 273.72 pm/MPa sensitivity with 0.0037-MPa resolution, alongside preserving high linearity over the range of 0–2 MPa. This design also presented low hysteresis and maintained a relative error of 2% after temperature compensation, demonstrating reliable pressure measurement performance. The cost-effective device shows potential capability to measure the pressure of gases or liquids in pipelines.

Acknowledgement

Project supported by the National Natural Science Foundation of China (Grant Nos. U2006217 and 62371035).

References

[1] Biezma M V, Andrés M A, Agudo D and Briz E 2020 *Eng. Fail. Anal.* **110** 104446
[2] Zawawi M A, O'Keffe S and Lewis E 2013 *Sens. Rev.* **33** 57
[3] Vorathin E, Hafizi Z M, Ismail N and Loman M 2020 *Opt. Laser Technol.* **121** 105841
[4] Ma G M, Jiang J, Mu R D, Li C R and Luo Y T 2015 *IEEE Photon. Technol. Lett.* **27** 177
[5] Liu H L, Zhu Z W, Zheng Y, Liu B and Xiao F 2018 *Opt. Fiber Technol.* **40** 144
[6] Wu W and Liu X 2015 *Optik* **126** 2411
[7] Zhang R, Pu S, Li Y, Zhao Y, Jia Z, Yao J and Li Y 2019 *IEEE Sens. J.* **19** 4079
[8] Hu W Y, Chen Z, You J S, Wang R H, Zhou R and Qiao X G 2023 *Chin. Phys. B* **32** 114201
[9] Wang D M, Lei Y H, Shi P F and Li Z A 2023 *Chin. Phys. B* **32** 090505
[10] Xu M G, Reekie L, Chow Y T and Dakin J P 1993 *Electron. Lett.* **29** 398
[11] Huang J, Zhou Z D, Wen X Y and Zhang D S 2013 *Measurment* **46** 1041
[12] Zhao Y, Zheng H K, Lv R Q and Yang Y 2018 *Sensor. Actuat. A-Phys.* **279** 101
[13] Zhu S Q, Liu M Y, Song H, Li C, Yang X L and Chen X C 2024 *Opt. Fiber Technol.* **84** 103694
[14] Fajkus M, Nedoma J, Martinek R, Fridrich M, Bednar E, Zabka S and Zmij P 2021 *Sensors* **21** 5158
[15] Xiong Y, He J, Yang W, Sheng L, Gao W and Chen Y 2012 *Proceedings of* 2012 *International Conference on Measurement, Information and Control*, May 18–20, 2012, Harbin, China, p. 787
[16] Chen L, Tong X L, Huang W Z, Zeng F C, Li C F, Wang Y H, Shi X F, Zeng C and Li Z K 2024 *Opt. Fiber Technol.* **84** 103743
[17] Li C F, Tong X L, Huang W Z, Wang Y H and Zeng F C 2024 *Opt. Fiber Technol.* **87** 103917
[18] Vorathin E, Hafizi Z M, Aizzuddin A M, Zaini M K A and Lim K S 2019 *Opt. Lasers Eng.* **117** 49
[19] Feng D Q, Xu D P, Chen F Y, Chen Q and Qiao X G 2023 *IEEE Sens. J.* **23** 3589
[20] Vaddadi V, Parne S R, Vijeesh V P, Gandi S, Panda S S S and Cenkeramaddi L R 2022 *IEEE Photonics J.* **14** 1
[21] Liu M Y, Cai Q H and Song H 2023 *Sensor. Actuat. A-Phys.* **355** 114298
[22] Liang M F, Fang X Q and Ning Y S 2018 *Photonic Sensors* **8** 157
[23] Burhanuddin W, Ahmad H, Alias M A, Sa'Ad M S M, Sun S F and Ismail M F 2024 *IEEE Sens. J.* **24** 25793
[24] Xu G, He B, Li H L, Gui X and Li Z Y 2022 *Opt. Express* **30** 21396
[25] Peng B J, Zhao Y, Yang H and Zhao M G 2005 *Measurement* **38** 176
[26] Thakar V C, Patel B N and Karsh P K 2022 *Materials Today: Proceedings* **65** 3683
[27] Nallathambi A, Shanmuganantham T and Sindhanaiselvi D 2018 *Materials Today: Proceedings* **5** 1897
[28] Devi R, Gill S S and Singh B 2022 *Meas.: Sens.* **24** 100522
[29] Jia Z A, Fan Q G, Feng D Q, Yu D K, Zhao X F and Yang K Q 2019 *Opt. Eng.* **58** 097109
[30] Fan Q G, Jia Z A, Feng D Q and Yong Z 2021 *Optik* **225** 165559
[31] Bao M H 2005 *Analysis and Design Principles of MEMS Devices* (Amsterdam: Elsevier) p. 103
[32] Wang Q and Ko W H 1999 *Sensor. Actuat. A-Phys.* **75** 230
[33] Sharma A and George P J 2008 *Sensor. Actuat. A-Phys.* **141** 376
[34] Sheng H J, Fu M Y, Chen T C, Liu W F and Bor S S 2004 *IEEE Photonics Technol. Lett.* **16** 1146
[35] Pachava V R, Kamineni S, Madhuvarasu S S, Putha K and Mamidi V R 2015 *Photonic Sensors* **5** 321
[36] Altenberger I, Kuhn H A, Müller H R, Mhaede M, Gholami-Kermanshahi M and Wagner L 2015 *International Journal of Materials & Product Technology* **50** 124
[37] Sun Y 2023 *Structures* **57** 105290
[38] Liu X B, Liang L, Jiang K and Xu G 2021 *IEEE Sens. J.* **21** 9155
[39] Hafizi Z M, Aizuddin A M and Vorathin E 2019 *IOP Conference Series: Materials Science and Engineering*, July 30–31, 2019, Kuantan, Malaysia, p. 012088
[40] Guo H Y, Wang Z B and Li H Y 2018 *J. Sens.* **2018** 2056452